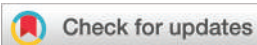


## PAPER

Cite this: *Nanoscale*, 2021, **13**, 19098

# Mesoporous thin films on graphene FETs: nanofiltered, amplified and extended field-effect sensing†

 Sebastián Alberti,<sup>‡a</sup> Esteban Piccinini,<sup>ID \*‡a</sup> Pedro G. Ramirez,<sup>b</sup> Gabriel S. Longo,<sup>ID a</sup> Marcelo Ceolín,<sup>ID a</sup> and Omar Azzaroni,<sup>ID a</sup>

The ionic screening and the response of non-specific molecules are great challenges of biosensors based on field-effect transistors (FETs). In this work, we report the construction of graphene based transistors modified with mesoporous silica thin films (MTF-GFETs) and the unique (bio)sensing properties that arise from their synergy. The developed method allows the preparation of mesoporous thin films free of fissures, with an easily tunable thickness, and prepared on graphene-surfaces, preserving their electronic properties. The MTF-GFETs show good sensing capacity to small probes that diffuse inside the mesopores and reach the graphene semiconductor channel such as H<sup>+</sup>, OH<sup>-</sup>, dopamine and H<sub>2</sub>O<sub>2</sub>. Interestingly, MTF-GFETs display a greater electrostatic gating response in terms of amplitude and sensing range compared to bare-GFETs for charged macromolecules that infiltrate the pores. For example, for polyelectrolytes and proteins of low MW, the amplitude increases almost 100% and the sensing range extends more than one order of magnitude. Moreover, these devices show a size-excluded electrostatic gating response given by the pore size. These features are even displayed at physiological ionic strength. Finally, a developed thermodynamic model evidences that the amplification and extended field-effect properties arise from the decrease of free ions inside the MTFs due to the entropy loss of confining ions in the mesopores. Our results demonstrate that the synergistic coupling of mesoporous films with FETs leads to nanofiltered, amplified and extended field-effect sensing (NAEXFES).

Received 8th June 2021,  
Accepted 14th October 2021  
DOI: 10.1039/d1nr03704h  
rsc.li/nanoscale

## Introduction

Field-effect transistor (FET) biosensors based on nanomaterials such as silicon nanowires,<sup>1</sup> conducting polymers<sup>2</sup> and graphene<sup>3</sup> offer outstanding capabilities for label-free high-sensitivity detection of biological species.<sup>4</sup> In the last decade, great progress has been made for scalable fabrication of nanomaterial-based FET sensors.<sup>5–7</sup> These devices show high sensitivity to diverse crucial biomarkers such as small biomolecules,<sup>8,9</sup> proteins,<sup>10</sup> antigens<sup>11</sup> and peptides,<sup>12</sup> among others. Interestingly, FETs can be designed in miniaturized and wireless format, and their output signal can be easily digi-

talized.<sup>13</sup> Despite all these advantages, the use of nanomaterial-based FETs for sensing in aqueous biological samples is still behind expectations. These sensors are primarily sensitive to the electrostatic potential induced by charged biomolecules adsorbed onto the semiconducting transistor channel or the gate electrode. Mobile ions present in the sample can effectively screen this electrostatic potential.<sup>14–16</sup> If the distance between the captured target biomolecule and the FET surface is larger than the electrostatic screening length (*i.e.*, the Debye length,  $\kappa^{-1}$ ), then, the sensor may become insensitive to this binding event.<sup>17</sup> Because  $\kappa^{-1}$  is below 1 nm under physiological conditions, there is a distance mismatch between the range of FET interfacial sensing and the size of most analytes.

To overcome this limitation, several strategies have been employed. For instance, a two-step method comprising an initial desalting step followed by protein detection in low ionic strength solution was reported.<sup>18</sup> This method allowed for efficient detection; however, the desalting step is not suitable for on-site and rapid detection. A high-frequency measurement method that can be applied to biological receptors was also reported.<sup>19,20</sup> While the sensitivity was indeed increased by

<sup>a</sup>Instituto de Investigaciones Físicoquímicas Teóricas y Aplicadas (INIFTA) – Departamento de Química, Facultad de Ciencias Exactas, Universidad Nacional de La Plata – CONICET, Suc. 4, CC 16, La Plata, Argentina.

E-mail: estebanpiccinini@inifta.unlp.edu.ar

<sup>b</sup>Instituto de Matemática Aplicada San Luis (IMASL), UNSL-CONICET, San Luis, Argentina

†Electronic supplementary information (ESI) available. See DOI: 10.1039/d1nr03704h

‡Joint first authors.

fading away the electric double-layer, the core problem of the electrostatic screening of the biomolecule charge still persisted. Lieber and co-workers reported that the effective screening length in the immediate proximity of the FET surface can be increased by the co-immobilization of the biorecognition element with a poly(ethylene glycol) layer.<sup>21,22</sup> Despite the potential of this approach,<sup>23</sup> the PEGylation of some nanomaterials can be a challenging task. For example, the immobilization of macromolecules on graphene is commonly realized by the use of monopyrenes (attached to graphene by weak  $\pi$ - $\pi$  interaction) presenting reactive pending groups (*e.g.*, -COOH, -NH<sub>2</sub>, -NHS) to avoid the disruption of the graphene aromatic chemical structure. Although the monopyrene linkers can efficiently retain some biomolecules,<sup>11,24</sup> they are susceptible to desorption if highly charged or hydrophilic molecules are bound.<sup>25-27</sup>

It is imperative to design versatile and robust interfacial strategies for on-site diagnostics that solve the problem of the mismatch between the Debye length and the reach of the biomarker-recognition element and, simultaneously, restrict the adsorption of non-relevant molecules that are present in biological samples. In this respect, mesoporous thin films (MTFs) present great potential because they contain ordered and monodisperse pore sizes in the range of 2–50 nm, so that the size filtration limit for non-specific molecules can be tuned.<sup>28-32</sup> Since mesopores present confined spaces of nearly molecular dimensions, the physical and chemical properties of the solution and chemical species inside the pores markedly differ from those exhibited in bulk. Of major interest is to incorporate two phenomena that these materials display into field-effect sensing devices. First, the concentration of counterion species inside charged MTFs (*e.g.* silica and titania films) drops considerably due to surface electrostatic repulsion, also known as Donnan potential exclusion.<sup>33-40</sup> This effect can be huge when the Debye length is larger than the pore size. Furthermore, there is a marked decrease of the electrolyte permittivity inside mesopores.<sup>41</sup> Both features may be harnessed to increase the surface potential change amplitude at the semi-conducting/conducting interfaces of FET devices.

The present work reports the construction of silica mesoporous thin films on reduced graphene oxide field-effect transistors (MTF-GFETs) with a specific design that combines the confined space properties of mesoporous materials with the advantages of FET sensors. To achieve that goal, firstly, the MTF coating and molding agent extraction steps are optimized to yield films free of fissures, and preserve the electronic properties of graphene. Complete structural characterization of the resulting MTFs prepared on reduced graphene oxide is performed. The film thickness, pore diameter distribution, porosity and pore-to-pore distance are obtained by ellipsometry, scanning electron microscopy (SEM), X-ray reflectivity (XRR) and grazing-incidence small-angle X-ray scattering (GISAXS), respectively. The electrolyte-gated transfer characteristic is studied by field-effect measurements. On the one hand, the interfacial sensing capacity of MTF-GFETs is evaluated by the use of small probes that can diffuse inside the mesopores

such as H<sup>+</sup>, OH<sup>-</sup>, dopamine and H<sub>2</sub>O<sub>2</sub>. On the other hand, polyelectrolytes and proteins of low and high molecular weight (that adsorb inside or outside the pores, respectively) are used to demonstrate the coupling of the MTF size-exclusion feature to the electrostatic gating GFET response. We find that MTF-GFETs display real-time nanofiltration properties and a marked amplified and extended response for charged molecules that adsorbed inside the pores. Finally, a thermodynamic model that describes the distribution of free ions and the Debye screening length inside the silica pores is derived to understand the interesting observations that result from MTF-GFETs.

## Experimental section

### Reagents

Linear polyethylenimine of 2.5 kDa (product number, 764604) and 10 kDa (product number, 765090), dopamine hydrochloride, tetraethoxysilane (TEOS), absolute ethanol, HEPES, and (3-aminopropyl)triethoxysilane (APTES) were purchased from Sigma Aldrich. Poly(4-styrene sulfonic acid sodium salt) of 12 kDa was purchased from Polymer Source Inc. H<sub>2</sub>O<sub>2</sub>, HCl, NaOH, KCl, NaCl, AcH, and AcNa were purchased from Anhedra. Lysozyme from chicken egg white (L6876, Sigma-Aldrich) was dialyzed with an Amicon centrifugal filtration tube (cut off = 10 kDa) before its use. Ultrapure water (18 M $\Omega$  cm<sup>-1</sup>) was used for the preparation of the solutions.

### Reduced graphene oxide field-effect transistors (GFETs)

Reduced graphene oxide (rGO) field-effect transistors were prepared as we reported in previous works.<sup>8,9,14</sup> The rGO acted as the transistor channel and an Ag/AgCl electrode was used as a gate. Liquid-gated GFET measurements were carried out using a batch-cell (from Micrux Technologies). For the FET transfer curves, the current between the source and drain electrodes ( $I_{DS}$ ) was measured as a function of the gate potential ( $V_G$ ) while the potential between the drain and the source ( $V_{DS}$ ) was fixed at 100 mV. Electrical measurements were performed by means of a Zaphyrus-W10 FET measurement station (GISENS BIOTECH, Argentina).

### Preparation of mesoporous thin films (MTF)

Silica mesoporous thin films were prepared on GFETs with a similar procedure as explained previously.<sup>42</sup> The preparation protocol comprises the following steps: (i) the precursor solution was prepared by mixing, under continuous stirring, prehydrolyzed Si(OEt)<sub>4</sub> (TEOS), molding agent, absolute ethanol and acidic water. The prehydrolyzed TEOS was prepared as explained before.<sup>43</sup> A triblock molding agent PNIPAM-*b*-P<sup>t</sup>butylacrylate-*b*-PNIPAM ( $M_n$  = 18 500 Da), polymerized in our laboratory,<sup>44</sup> was used to fabricate MTF with a pore diameter of approximately 18 nm. The following final composition was used to obtain films without cracks: 1 TEOS : 0.004 PNIPAM-*b*-P<sup>t</sup>BA-*b*-PNIPAM : 40 EtOH : 10 H<sub>2</sub>O : 0.01 HCl (molar ratio); (ii) the precursor solution was deposited on the semiconductor

channel and/or the gate electrode of the FETs using the spin-coating technique. Different angular speeds (ranging from 1000 to 3000 RPM) for 10 minutes were used to achieve different MTF thicknesses (ranging from 100 to 300 nm); (iii) the molding agents were extracted by calcination at 360 °C for 1 hour under an atmosphere of N<sub>2</sub>. This protocol allows the extraction of the molding agent from the MTF without deteriorating the electrical properties of the semiconductor material.

### Grazing-incidence small-angle X-ray scattering (GISAXS)

GISAXS and XRR measurements were performed with a Xeuss 1.0 (Xenocs, France) setup. The wavelength of the X-ray micro-focus source was 0.15419 nm and the scattered beam was detected using a Pilatus 100 K (DECTRIS Ltd, pixel size of 0.172 mm × 0.172 mm) detector at a distance of 2500 mm from the sample. Mesoporous thin films were prepared on rGO-modified Si (100) wafers. To achieve that, Si wafers were modified with a 2% APTES ethanolic solution for 1 h and, then, GO was adsorbed and chemically reduced as described in previous works.<sup>8,9</sup> The critical angle for total reflection of the MTF ( $\alpha_{c,MTF}$ ) was obtained by XRR measured at 0% relative humidity (RH). Critical angles were obtained from the critical momentum transfer,  $q_c$ , by the equation  $q_c = 4\pi \sin(\alpha_c)/\lambda$ . The porosity was deduced from  $\alpha_{c,MTF}$  as described by Gibaud and co-workers.<sup>45</sup>

In order to maximize the GISAXS information coming from the internal film structure, an incident angle of  $\alpha_i = 0.15^\circ$  was chosen, between the critical angle for total reflection of the mesoporous film,  $\alpha_{c,MTF} = 0.147^\circ$ , and the critical angle of the Si substrate,  $\alpha_{c,Si} = 0.226^\circ$ . To obtain the pore center-to-center distance ( $D_{p-p}$ ), the GISAXS scattering pattern was cut along  $q_z$  (out-of-plane), and its intensity profile was analysed by fitting to Gaussian functions so that the peak position ( $q_p$ ) of the predominant structure can be determined.<sup>46,47</sup> Then, the following equation was used:<sup>48,49</sup>

$$q_p = \frac{2\pi}{\lambda} \left( \sin(\alpha_i) + \sqrt{\sin^2(\alpha_{c,MTF}) + \left[ \frac{m\lambda}{D_{p-p}} \pm \sqrt{\sin^2(\alpha_i) - \sin^2(\alpha_{c,MTF})} \right]^2} \right) \quad (1)$$

where  $\lambda$  is the wavelength of the beam,  $\alpha_i$  is the incidence angle of the X-ray beam with respect to the film surface, and  $m$  is the order of the reflection. FITGISAXS software was used for data analysis.<sup>50</sup>

### Ellipsometry

Ellipsometric measurements were performed with an  $\alpha$ -SE ellipsometer (from Woollam Co. Inc.) and using Si wafer substrates modified with rGO. A multilayer Cauchy model taking into account the layers of different materials was used (see Table S1†). To obtain the thickness and/or the optical parameters for each Cauchy layer, ellipsometric measurements were performed after each modification step and fitted with

the CompleteEASE software.<sup>51</sup> Then, mesoporous thin films were prepared on rGO-modified Si and the MTF thickness was estimated using a Bruggeman effective medium approximation with a fitting model with two components: void and silica.<sup>52</sup> The “goodness” of the fits was evaluated on the basis of the mean squared error (MSE).

### Scanning electron microscopy

Scanning electron microscopy (SEM) images were recorded in order to study the mesoporous thin film modification of rGO substrates and rGO-FETs. A SUPRA 40 Field Emission Scanning Electron Microscope (Zeiss) was used.

### Evaluation of the nanofiltration property of MTF-GFETs

The nanofiltration capacity of mesoporous thin films prepared on rGO-FETs was studied by using molecules of different sizes. To evaluate the diffusion of molecules into the MTF and their arrival to the sensorial graphene surface, the MTF-GFET electronic properties were studied in the presence of different small ions and molecules: (i) H<sup>+</sup>; (ii) dopamine and (iii) hydrogen peroxide (H<sub>2</sub>O<sub>2</sub>). On the other hand, to prove the size exclusion MTF properties, polyelectrolytes (PEs) of different molecular weights were used: 2.5 kDa and 10 kDa polyethylenimine (PEI), and 12 kDa poly(sodium 4-styrenesulfonate) (PSS). Moreover, to monitor step-by-step the loading of the pores, MTF-GFETs were modified with PEI and PSS by using the layer-by-layer nanoconstruction technique. Briefly, the substrates were incubated alternately in 2 mg ml<sup>-1</sup> PEI and 2 mg ml<sup>-1</sup> PSS. The PE aqueous solutions were prepared in the presence of 0.5 M KCl at pH 8 (adjusted with KOH). After incubating the substrates in the respective polyelectrolyte solution for 25 min, they were rinsed with deionized water and dried with N<sub>2</sub>. For the assembly of polyelectrolytes onto the bare graphene, the rGO surfaces were first modified with sodium 1-pyrenesulfonate to obtain a negatively charged basic layer as reported previously.<sup>14</sup> In this process, the pyrene groups attach to graphene through  $\pi$ - $\pi$  interactions whereas the oppositely positioned sulfonate groups form a negatively charged surface.<sup>8</sup> The electronic response of MTF-GFET was also studied after the incubation of the sensors in 2 mg ml<sup>-1</sup> lysozyme (MW = 14.3 kDa, pI = 11.3), a protein smaller than the pore size, for 20 minutes in 25 mM AcH/AcNa buffer and 115 mM NaCl.

### Calculation of the free ion distribution inside the MTF by a thermodynamic model

To investigate the distribution of ions inside the silica nanopores, we apply a recently developed thermodynamic theory.<sup>53</sup> The system we model consists of a thin film of silica having a pore of radius  $R = 10$  nm connecting two regions of an aqueous solution that contains water, hydroxyl ions, hydrogenium ions and KCl assumed to be completely dissociated into potassium cations and chloride anions. Solution species are excluded from the solid material, which has relative dielectric permittivity  $\epsilon = 3.9$ . The thickness of the silica film (or the pore depth) is  $h_{\text{film}}$ . The center of the pore sets the origin of

our cylindrical coordinate system. The upper ( $z = h_{\text{film}}/2$  and  $r > R$ ) and bottom surfaces of the silica film are planar while the pore surface ( $-h_{\text{film}}/2 \leq z \leq h_{\text{film}}/2$  and  $r = R$ ) is cylindrical. On these solution-exposed surfaces the charge density is  $\sigma = 4.5 \times 10^{-3} \text{ C m}^{-2}$ .<sup>54</sup> There is symmetry over the  $z$ -axis, and we also impose reflection symmetry with respect to the  $z = 0$  plane. Thus, we will only present results for a position  $(r, z)$  such that  $z \geq 0$ . The film thickness is sufficiently large so that near the center of the pore the density of each solution species only depends on the radial coordinate.

Next, we briefly describe the theoretical approach, while the full description can be found in the literature.<sup>53</sup> The Helmholtz free energy of the system is:

$$F = -TS_t + U_E$$

where  $T$  is the temperature and  $S_t$  is the translational entropy of solution species, which also includes the self-energies of these molecules;  $U_E$  is the electrostatic energy. These contributions to the free energy can be expressed in terms of (i) the local densities of the solution species and (ii) the electrostatic potential. Minimization of the appropriate thermodynamic potential with respect to these functions (i and ii) yields explicit expressions for the densities in terms of two interaction potentials, the osmotic pressure and the electrostatic potential. The extremum of the free energy with respect to the electrostatic potential yields the Poisson equation in different regions

of space as well as the boundary conditions at the charged silica surfaces. The interaction potentials can be obtained through solving the Poisson equation and the incompressibility constraint, which requires every element of volume in the solution to be fully occupied by some of the chemical species. This last constraint incorporates the steric interactions between molecules at the excluded-volume level. Once these interaction potentials are numerically calculated at each point in space, the local densities of all solution species can be derived from the minimized thermodynamic potential.

## Results and discussion

### Characterization of mesoporous thin films (MTF) on rGO

Mesoporous thin films (MTF) were prepared on rGO-FETs as illustrated in Fig. 1a and d. PNIPAM-*b*-P<sup>+</sup>BA-*b*-PNIPAM, a triblock polymer, was used as the mesogenic agent of the mesoporous architecture, and TEOS as the silica precursor. Thus, MTFs of a large pore diameter with well-connected pores were obtained. Scanning electron microscopy (SEM) studies were performed for the characterization of GFETs before (Fig. 1a-top) and after the MTF deposition (Fig. 1a-bottom). The pore size distribution was obtained from the SEM image (Fig. 1b) and an in-plane pore size ( $D_p$ ) of 17.9 nm was estimated. The sol-gel formulation was optimized to obtain MTF films (see the side view SEM image in Fig. S1a†) on rGO surfaces with

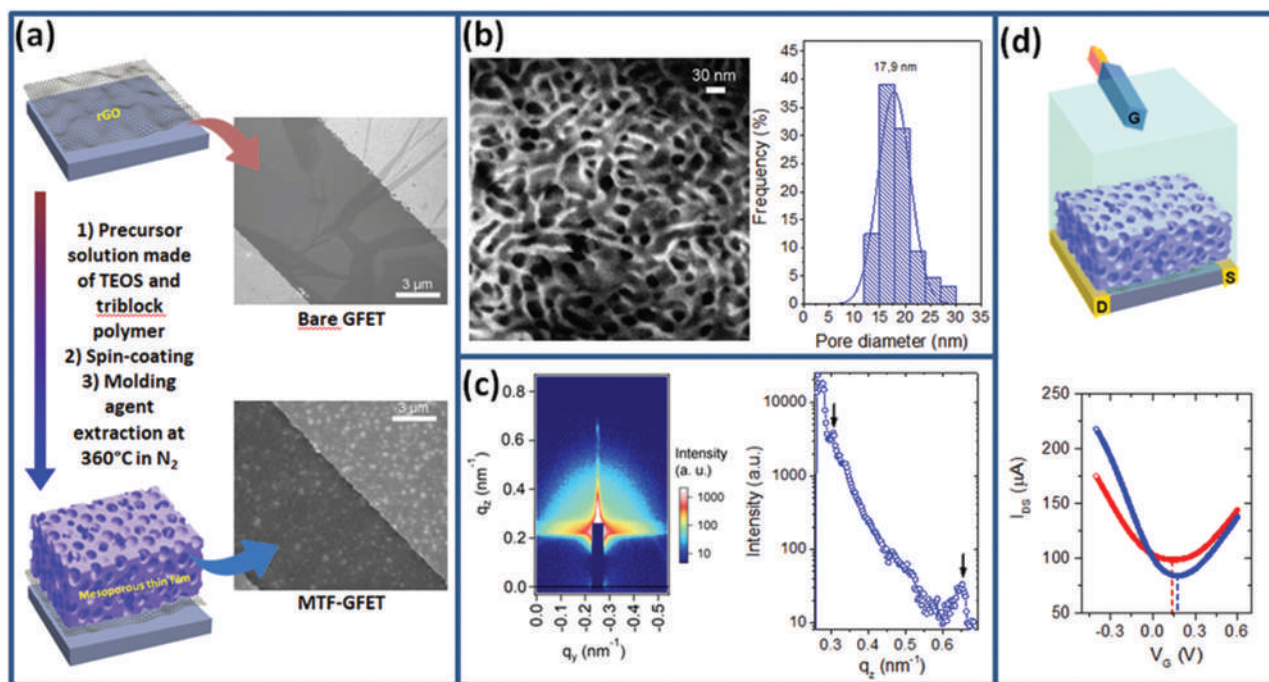


**Fig. 1** (a) Schematic of the mesoporous thin film (MTF) preparation on a reduced graphene oxide field-effect transistor (GFET). Scanning electron micrograph (SEM) of a GFET before and after the MTF preparation made of PNIPAM-*b*-P<sup>+</sup>BA-*b*-PNIPAM as the mesogenic agent, and TEOS as the silica precursor. (b) Magnified top-view SEM image of a MTF-GFET and its respective pore diameter distribution. (c) GISAXS pattern of a MTF prepared on rGO (left) and out-of-plane intensity profile (right). Sample-to-detector distance: 2500 mm, wavelength: 0.15419 nm, angle of incidence: 0.15°. (d) Schematic of the measuring configuration for an electrolyte-gated MTF-GFET. Transfer characteristics of a bare GFET (red line) and a MTF-GFET (blue line) measured in 2 mM KCl and 0.1 mM HEPES pH 7.0 solution.

good film adhesion (see the adhesion test in Fig. S1b†) and without the appearance of fissures in the MTFs. It is worth noting that a complete MTF covering of semiconductor surfaces is a crucial feature for the presence of nanofiltered and extended field-effect sensing properties. On the other hand, MTFs with fissures, which can be observed for inaccurate formulations (Fig. S1c†), may display deficient sensing properties.

The internal structure of MTFs prepared on rGO surfaces was studied by grazing-incidence small-angle X-ray scattering (GISAXS). The GISAXS scattering pattern and its profile along the  $q_z$  axis (out-of-plane) are presented in Fig. 1c. The pore center-to-center ( $D_{p-p}$ ) distance was obtained from the Bragg diffraction peak of the out-of-plane profile and calculated using eqn (1).<sup>38,47</sup> The MTF displayed a Bragg diffraction peak at  $q_z = 0.305 \text{ nm}^{-1}$ , evidencing a  $D_{p-p}$  of 24.4 nm. A second and less intense diffraction peak is presented at  $q_z = 0.65 \text{ nm}^{-1}$  evidencing an interpore (neck-to-pore) characteristic spacing of 10.4 nm. Spectroscopic ellipsometry has been used to determine the MTF thickness (Fig. S2†), which can be controlled by adjusting the angular velocity of the spin-coating preparation. For example, MTF prepared on rGO surfaces at angular speeds of 1000, 2000 and 4000 rpm displayed thicknesses of 250, 207 and 135 nm, respectively (Fig. 2a). The percentage residual

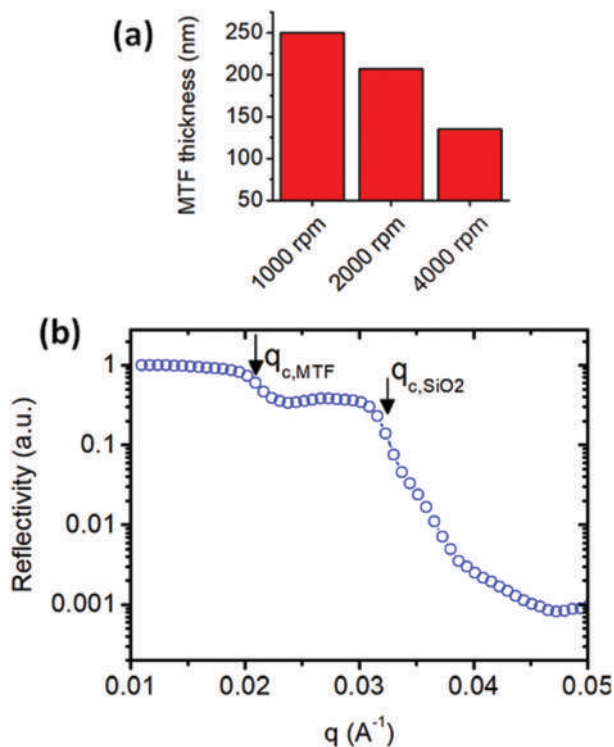


Fig. 2 (a) MTF thickness, measured by ellipsometry, as a function of the spin-coating angular speed. The multilayer model used for fitting the ellipsometric results is detailed in the ESI.† (b) XRR data corresponding to the MTF on rGO. In order to obtain accurate density values, measurements were performed under low-humidity conditions by using a continuous flow of dry nitrogen. The critical momentum transfer,  $q_c$ , is indicated for the MTF and the Si wafer substrate.

porosity after thermal treatment at 360 °C under a  $\text{N}_2$  atmosphere was obtained by XRR (Fig. 2b), and a value of  $56 \pm 3\%$  was estimated.

### Field-effect characterization of MTF-modified graphene field-effect transistors (MTF-GFETs)

The field-effect properties of rGO-FETs with an electrolyte-gated configuration were studied. As can be appreciated in Fig. 1d, upon the MTF coating, the transfer characteristics ( $I_{\text{DS}}-V_{\text{G}}$  plot) of the transistor resulted in a higher transconductance and a shift of the charge neutrality point potential ( $V_{\text{CNP}}$ , also referred to as the Dirac point) to more positive  $V_{\text{G}}$  potential. The increase of the transconductance (or the charge carrier mobility) may be related to the calcination treatment, as was described previously for high temperature annealing of rGO FETs.<sup>55,56</sup> On the other hand, the  $V_{\text{CNP}}$  shift could be yielded by the electrostatic gating induced by the silica MTF negative charge.<sup>57</sup> It should be highlighted that the extraction of the molding agent from mesoporous films was carried out without deterioration of the rGO electrical properties. As can be appreciated in the literature, the extraction of MTF molding agents is normally carried out at temperatures between 400 and 500 °C.<sup>29,58</sup> High temperature treatments of FETs may result in a worsening of electrical properties of the semiconductor materials, in particular if conducting polymers or semiconducting small molecules are used.<sup>59,60</sup> We overcome this problem with a double-approach: (i) the use of graphene, a material with great chemical stability, for the transistor channel; (ii) the calcination at lower temperatures (360 °C) in a  $\text{N}_2$  atmosphere to avoid the rGO oxidation.

### MTF-GFET response to small molecules

Owing to their defective structure and the remaining functional groups of reduced-graphene oxide, rGO-FETs are advantageous for pH sensing.<sup>8,61,62</sup> The FET transfer characteristic dependency on the pH value is caused mainly by the changes in the surface charge density by the protonation or deprotonation of the remaining functional groups at the rGO surface and below it, such as  $-\text{OH}$  and  $-\text{COOH}$  groups from rGO, and  $-\text{SiO}_2$  and  $-\text{NH}_2$  from the glass substrate modified with APTES.<sup>63,64</sup> This inherent property of rGO-FETs is an interesting tool that can be used to study the interface between rGO and MTF. In particular, it may shed light on the nature of the electrolyte solution inside the MTF pores that is in intimate contact with the rGO.

The transfer characteristics of the transistors were studied in a liquid-gated configuration under different pH values. Fig. 3b shows the  $I_{\text{DS}}-V_{\text{G}}$  curves of a MTF-GFET in solutions with constant ionic strength and pH ranging from 2 to 8. Whereas the hole and electron transconductance remained almost unchanged, a significant shift of the charge neutrality point ( $V_{\text{CNP}}$ ) to more positive  $V_{\text{G}}$  upon increasing the pH value was observed. A pH sensitivity of 44.3 mV per pH ( $R = 0.975$ ) was estimated, in concordance to those reported for bare GFETs.<sup>8,9,65</sup> The pH response for MTF-GFETs evidences that part of the rGO is in contact with the electrolyte solution

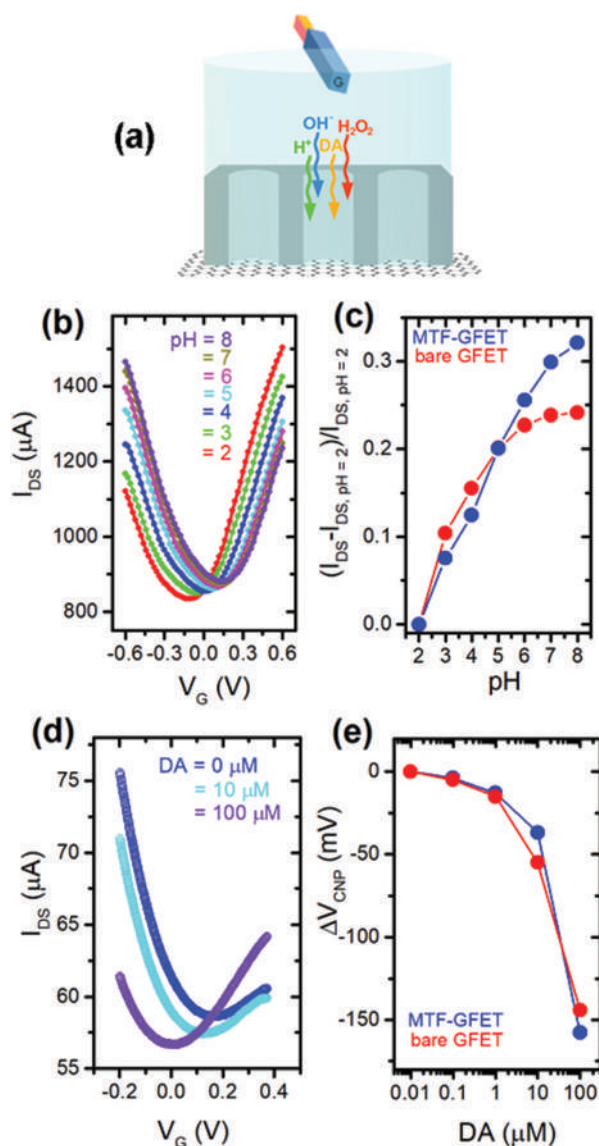


**Fig. 3** (a) Illustration of small probe infiltration inside the mesoporous film prepared on a GFET (b)  $I_{DS}$ - $V_G$  curves for a MTF-GFET at pH values ranging from 2 to 8. (c) Comparison of the  $I_{DS}$  response (at a  $V_G = -400$  mV) as a function of pH for a GFET before (red) and after (blue) being modified with a silica MTF. (d) Transfer characteristic for a MTF-GFET at different dopamine (DA) concentrations (from 0 to 100 μM). (e)  $\Delta V_{CNP}$  for a bare-GFET (red) and a MTF-GFET (blue) as a function of DA concentration. Experiments were carried out in PBS  $\times 1$  buffer (pH 7.4, ionic strength 140 mM) using an Au-gate also modified with MTF.

inside the MTF pores, a requirement for high output field-effect sensing. Fig. 3c compares the pH response for a GFET before and after being coated with a MTF. An increase in sensitivity to pH variation and an improvement in linearity can be seen for the case of the GFET coated with MTF. These results proved that rGO-FETs do not lose their interfacial sensing features after MTF coating.

Dopamine, a biomarker that plays an important role in the functions of the central nervous system which can be detected

by GFETs,<sup>66</sup> was also used to evaluate the MTF-GFET response in physiological-like solutions. For this purpose, Au floating-gate GFET sensors were measured in the presence of different concentrations of dopamine (DA). Fig. 3d shows the  $I_{DS}$ - $V_G$  curves for a MTF-GFET measured at 0, 10 and 100 μM DA prepared in PBS. As can be seen, the transfer characteristic plots show a shift of  $V_{CNP}$  towards more negative  $V_G$  potentials as the dopamine concentration increases (Fig. 3e). The response of the device with an Au-gate electrode is due to the electrochemical reaction of DA at the gate, *i.e.* the DA electro-oxidation to *o*-dopaminequinone, yielding large  $V_{CNP}$  shifts.<sup>66,67</sup> As was previously described,<sup>66</sup> the electrochemical reaction of DA at the Au-gate electrode decreases the potential drop at the interface because of the faradaic current. Consequently, the voltage applied on the electrolyte/graphene interface is increased, which leads to the increase of the effective gate voltage applied on the GFET and the shift of the  $I_{DS}$ - $V_G$  curve to a lower  $V_G$ . From our results, it can be inferred that dopamine diffuses along the mesopore channels allowing detection by the gate of the transistor.

Finally, the electrochemical response of the MTF-GFET sensors was studied in electrolytic solutions in the absence and the presence of H<sub>2</sub>O<sub>2</sub> (Fig. S3-left†). The transfer characteristic curves show a non-significant variation of the  $V_{CNP}$ , but a change in transconductance of the hole branch. This response is evidenced as a decrease of  $I_{DS}$  upon increasing the H<sub>2</sub>O<sub>2</sub> concentration in real-time measurements, *i.e.* with fixed potentials  $V_G = -400$  mV and  $V_{DS} = 100$  mV (Fig. S3-right†). These results are in agreement with GFET responses previously reported by other authors.<sup>68</sup> From these results it is demonstrated that small compounds such as protons, hydroxyl, DA and H<sub>2</sub>O<sub>2</sub> diffuse through the mesoporous film and can be detected by the gate or rGO channel transistor.

### Nanofiltered, amplified and extended field-effect sensing (NAExFES) with MTF-GFETs

Mesoporous films can avoid the entrance of molecules by size exclusion in the size range of 2–50 nm, depending on the pore diameter.<sup>30,31</sup> Therefore, when MTFs are prepared on the GFETs, real-time nanofiltration properties may be shown. To demonstrate this point, the adsorption of polyanions and polycations of different molecular weight (MW) inside the MTFs was used as a study model. To do so, MTF-GFETs were modified with 2.5 kDa PEI and 12 kDa PSS (termed, lowest MW PEs) or 10 kDa PEI and 12 kDa PSS (termed, highest MW PEs) by the layer-by-layer (LbL) adsorption technique. As previously described,<sup>69</sup> two different scenarios of modification are observed depending on the PE molecular weights. On the one hand, by using the lowest MW PEs, the polyelectrolytes are able to infiltrate inside the pores. On the other hand, by using the highest MW PEs, the modification occurs only on the external surface of the mesoporous film. Based on these scenarios, three systems were studied to prove the MTF-GFET nanofiltered sensing behaviour: (i) as a control experiment, PEI/PSS multilayer assemblies were constructed on a bare GFET (Fig. 4a); (ii) high MW PEI/PSS multilayer assemblies were pre-

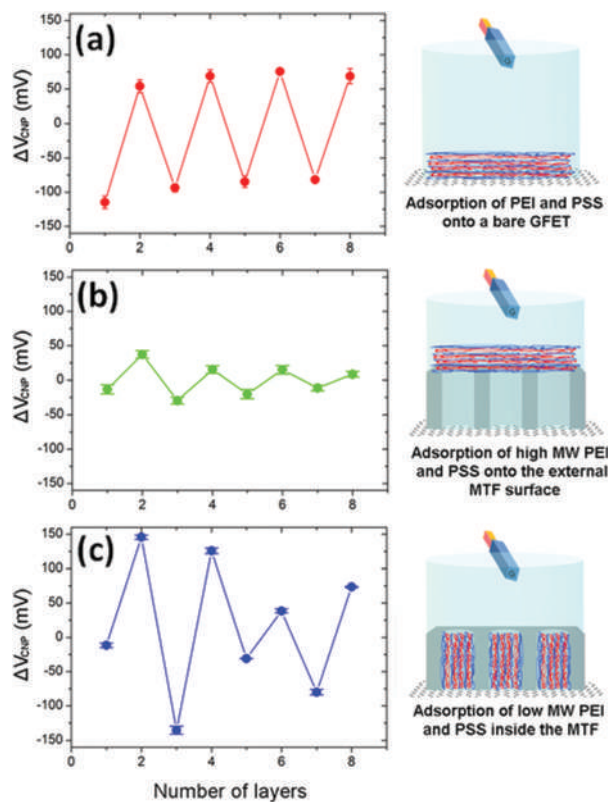


**Fig. 4** Change of the Dirac point ( $\Delta V_{\text{CNP}}$ ) as a function of the number of polyelectrolyte layers for (a) a bare GFET; (b) a MTF-GFET modified with high MW (and size excluded) polyelectrolytes that only adsorb onto the external film surface; (c) a MTF-GFET modified with low MW polyelectrolytes that infiltrate and adsorb inside the mesoporous structure. Field-effect measurements were performed in a 2 mM KCl solution using an Ag/AgCl gate electrode.

pared on MTF-GFETs (Fig. 4b); (iii) low MW PEI/PSS multilayer assemblies were prepared inside MTF-GFETs (Fig. 4c).

After cycling incubation of GFETs in the polyelectrolyte solutions for 25 min (each cycle), they were rinsed with deionized water and dried with  $\text{N}_2$  and  $I_{\text{DS}}-V_{\text{G}}$  measurements were carried out at 2 mM KCl. The assembly of a positively charged PEI layer onto the bare GFET resulted in a  $V_{\text{CNP}}$  shift to a more negative gate voltage. In contrast, the subsequent negatively charged PSS layer displaced  $V_{\text{CNP}}$  to a more positive gate voltage. An explanation has been described in previous works, which ascribe this field-effect behavior to the induction of negative (positive) charges on graphene induced by the adsorption of positively (negatively) charged macromolecules.<sup>14,16,57</sup> Dirac point shifts of approximately  $-100$  mV and  $+75$  mV were recorded after the polycation and the polyanion were adsorbed, respectively. For the first 4 bilayers, the shift of  $V_{\text{CNP}}$  was almost completely reversible after each layer. This is due to the well-known charge overcompensation behavior of polyelectrolyte LbL assemblies.<sup>70</sup> These results are in agreement with PDADMAC/PSS LbL assemblies reported previously.<sup>14,16</sup>

If high MW PEI/PSS multilayer assemblies are prepared with the MTF-GFETs (Fig. 4b), small  $V_{\text{CNP}}$  variations are dis-

played. These observations evidence the exclusion of high MW macromolecules provided by the mesoporous film, which are in concordance with optical wave spectroscopy (OWS) results as previously reported.<sup>69</sup> Interestingly, for assemblies capable of infiltrating the porous matrix (*i.e.*, by using the PEs of lowest MW), two stages of behavior are observed (Fig. 4c). The first one (up to the fourth layer) presents large  $\Delta V_{\text{CNP}}$  values after each PE layer assembly. This stage coincides with the adsorption of the PEs inside the pores, as reported previously by OWS.<sup>69</sup> Furthermore, since the  $\Delta V_{\text{CNP}}$  responses are higher than those obtained for bare GFETs (see Fig. 4a and c), it can be inferred that an amplified sensing is presented for charged macromolecules that adsorb inside MTF-GFETs. The second one (above the fourth layer) involves an important diminution of  $V_{\text{CNP}}$  shifts and occurred after the MTF pore were completely filled and, thus, PEs could only adsorb on the outer MTF surface. It should be noted that after the pores are completely filled, an abrupt increase of the distance between the outermost polyelectrolyte layer and the graphene surface takes place. Nevertheless, the  $V_{\text{CNP}}$  oscillations did not turn off completely once the MTF was completely filled. This means that these field-effect devices can still sense surface charge changes at a distance of 250 nm, more than 35 times higher than the Debye length of the electrolyte used (*i.e.*, 6.8 nm), evidencing an important extension of the field-effect.

The polyelectrolyte responses for MTF-GFETs prepared with mesoporous films of different thicknesses were studied. For each system, an average  $\Delta V_{\text{CNP}}$  was calculated for the LbL modification before (considering the second layers) and after (considering the sixth layers) the complete loading of the pores (observed consistently after the deposition of the fourth layer). Fig. 5a shows the drop in  $\Delta V_{\text{CNP}}$  after filling the pores as a function of the MTF thicknesses. It is clear that the thicker the MTF film, the higher the drop in  $\Delta V_{\text{CNP}}$  value, suggesting that as the MTF film gets thicker, the amplification and extension of the field-effect get more pronounced.

To assess the MTF-GFET response for the infiltration of proteins, we used lysozyme (Lyz), a small positively charged protein (MW = 14.3 kDa and IP = 11) prone to be adsorbed inside mesoporous silica.<sup>71,72</sup> Transfer characteristic curves for GFETs with and without MTFs (*i.e.*, positive and control systems) were recorded at 140 mM ionic strength before and after incubating in a lysozyme solution (Fig. 5b and Fig. S4,† respectively). A small  $V_{\text{CNP}}$  change of approximately  $-6$  mV was obtained for the bare GFET, probably due to the use of an almost physiological ionic strength with a Debye screening length  $< 1$  nm, smaller than the protein size (lysozyme diameter  $\sim 3-4$  nm). On the other hand, MTF-GFETs displayed a  $V_{\text{CNP}}$  shift of  $-12.5$  mV after lysozyme incubation. Therefore, as for low MW polyelectrolytes, a nanofiltered, amplified and extended field-effect sensing (NAExFES) was observed when an MTF is coupled to GFETs, as depicted in Fig. 5c.

### Thermodynamic model

To shed light on the properties of amplification and extension of the field-effect that originates from coupling a mesoporous

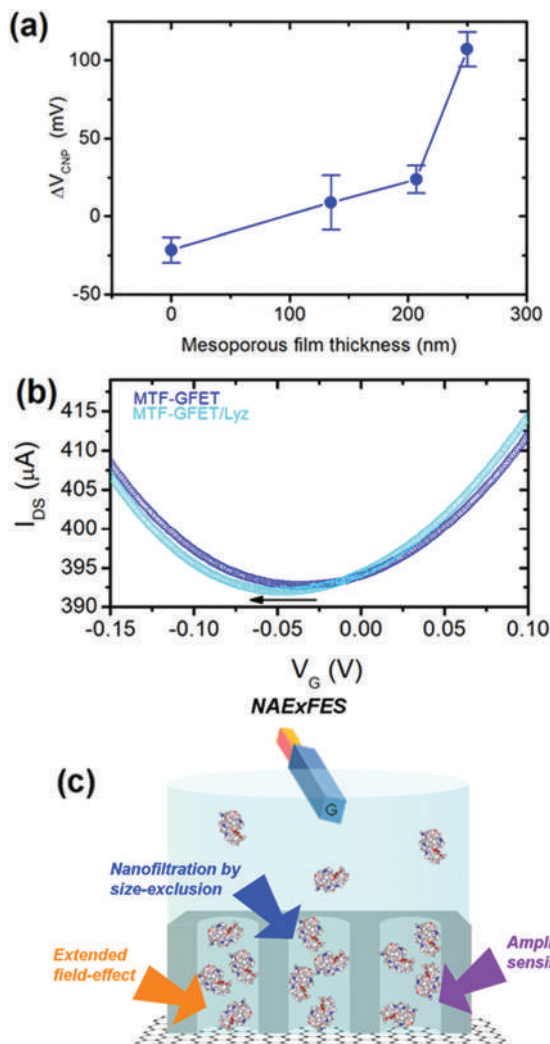


**Fig. 5** (a) Drop in  $\Delta V_{\text{CNP}}$  after the complete pore loading for MTF-GFETs prepared with different mesoporous film thicknesses. The field-effect measurements were performed in a 2 mM KCl solution using an Ag/AgCl gate electrode. (b)  $I_{\text{DS}}-V_{\text{G}}$  curves for MTF-GFET sensors before (blue) and after (light blue) lysozyme adsorption. The experiments were carried out using an Ag/AgCl gate, and Ach/AcNa-NaCl buffer (pH = 5, ionic strength = 140 mM) and applying  $V_{\text{DS}} = 100$  mV. (c) Illustration of nanofiltered, amplified and extended field-effect sensing (NAExFES) presented in MTF-GFETS.

film to field-effect devices, a thermodynamic model to describe the distribution of ions inside the silica mesopores was derived. The ionic strength in the vicinity of and inside a silica nanopore, with a pore radius of 10 nm, in the presence of 2 and 100 mM KCl electrolyte solutions is shown in Fig. 6a and Fig. S5,† respectively. To calculate these results we have considered the ionic strength of free ions ( $I_{\text{F}}$ ), namely, the local concentration excess of potassium counterions is considered bound to the surface to render electroneutrality (Fig. S6†). At 2 mM KCl, the ionic strength inside the pore drops to 0.47 mM at the pore center and 0.03 mM at the internal pore wall. This effect results from the entropy loss of confining the ions inside the pore, as the local (solution)

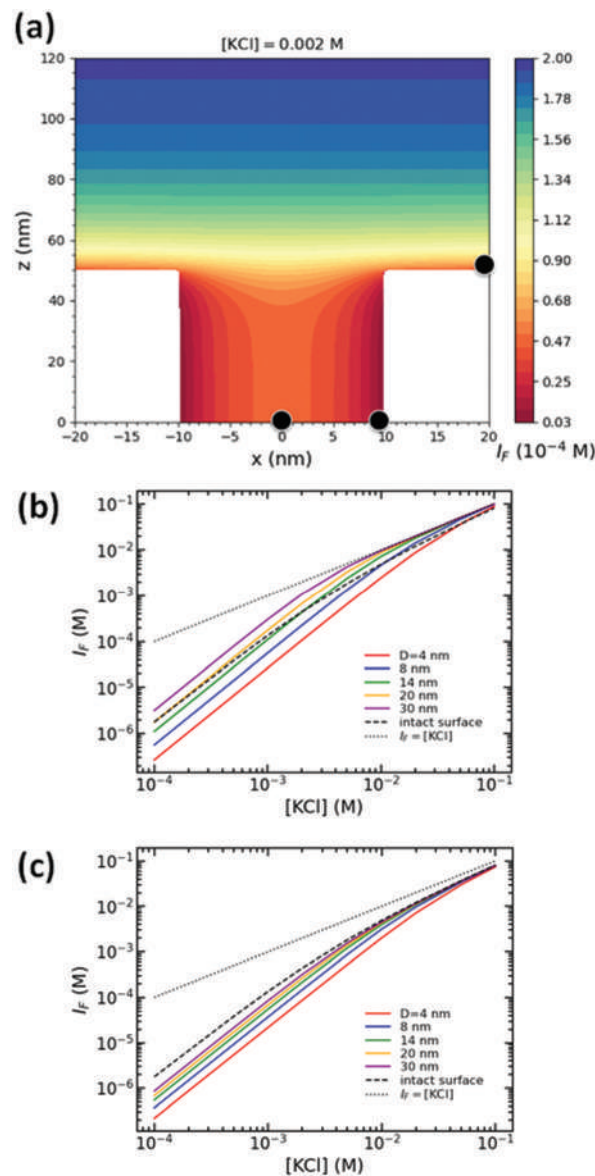


**Fig. 6** (a) Contour plots of the ionic strength of free ions ( $I_{\text{F}}$ ) for a 10 nm radius silica pore at 2 mM KCl and pH 7, as predicted by our thermodynamic model. The white region denotes the silica. In this side view of the pore, Cartesian coordinate  $x$  is plus/minus the radial coordinate  $r$ . Three positions are marked with black dots: the center of the pore ( $r = 0, z = 0$ ), the inner cylindrical pore surface ( $r = 10, z = 0$ ) and the external intact planar surface ( $r = 20$ , sufficiently far from the pore center,  $z = \text{external film surface}$ ).  $I_{\text{F}}$  at the center of the pore (b) and the internal wall (c) as a function of the bulk ionic strength for silica pores of diameters ranging from 4 to 30 nm.  $I_{\text{F}}$  at the intact surface is independent of pore size.

volume is largely occupied by bound potassium ions. As can be seen in Fig. 6b and c, the effect becomes stronger as the nanopore radius decreases, but becomes weaker as the bulk ionic density increases. Although the effect strongly decreased at the center of the pore ( $r = 0$ ) for bulk salt concentration larger than 100 mM, it remains significant at the inner cylindrical pore wall (Fig. 6a and Fig. S5†).

From these results it is evident that the effective Debye length ( $\kappa^{-1}$ ) inside the pores is higher than that of the bulk solution. For instance, at 2 mM KCl,  $\kappa^{-1}$  is 6.8 nm for the bulk solution, while it is 14 nm at the center of the pore and 55.5 nm at the inner pore wall. This increase of the effective Debye screening length inside the pores obtained by our thermodynamic model explains the extended field-effect property observed for MTF-GFETs. Moreover, to give a qualitative understanding of the amplification effect, the Grahame equation that relates the surface charge density ( $\sigma$ ) to surface potential ( $\psi_s$ ) for charged surfaces in electrolyte solutions can be used.<sup>73</sup> Rearranging the Grahame equation, and considering a symmetric valency electrolyte, provides the following expression for the surface potential at the graphene surface:<sup>74</sup>

$$\psi_s = \frac{2k_b T}{ez} \arcsin h \left( \frac{\sigma}{\sqrt{8n\epsilon_r \epsilon_0 k_b T}} \right)$$

where  $e$  is the elementary charge,  $\epsilon_0$  is the permittivity of free space,  $\epsilon_r$  is the relative permittivity of the medium,  $z$  is the valence of the electrolyte ions (of symmetric valence),  $n$  is the number density of electrolyte in the medium (*i.e.*, in the bulk solution or inside the mesopore),  $k_b$  is the Boltzmann constant and  $T$  is the temperature. Since the decrease of electrolyte ions yields larger  $\psi_s$ , it is inferred that the amplification sensing effect observed in the field-effect measurements derives from the diminution of free ions inside the pores. Although  $\epsilon_r$  changes were not taken into account in our thermodynamic model, a decrease of this value inside the pores, as reported in previous literature,<sup>41</sup> may also favor the amplification sensing effect.

## Conclusion

In summary, silica mesoporous thin films were prepared on graphene-based FETs for electrolyte-gated measurements. The MTF coating and molding agent extraction steps were optimized to yield MTF-GFETs free of fissures, and preserve the electronic properties of graphene. By the use of small probes ( $H^+$ ,  $OH^-$ , dopamine and  $H_2O_2$ ), that can diffuse inside the mesopores, it was evidenced that the interfacial sensing capacity of the graphene-based FETs remained after being coated with MTFs. Moreover, MTF-GFETs showed a greater electrostatic gating response (than the bare-GFETs) for polyelectrolytes and proteins of low MW that could enter the pore, but smaller electrostatic gating for macromolecules of high MW that were size-excluded and only adsorbed onto the MTF external surface. Therefore, our results evidence that unique properties such as size-exclusion filtration, signal amplification and extension of the field-effect are seen for field-effect devices modified with porous membranes. Finally, a thermodynamic model that describes the distribution of free ions inside the silica pores indicated that amplification and extended field-effect properties arise from the decrease of free ions (*i.e.*, the increase of the Debye screening length) inside the MTFs due to the entropy loss of confining the ions inside the pore. We believe that this combination of dielectric meso-

porous materials and field-effect devices that lead to nanofiltered, amplified and extended field-effect sensing (NAExFES) will have profound implications in the fields of whole biological sample biosensing without the use of purification or sample treatments.

## Author contributions

E. P. prepared the initial draft. The final manuscript was written through contributions of all authors. All authors have given approval to the final version of the manuscript. S. A. and E. P. designed and developed the technology, prepared MTF samples and MTF-FETs, conducted experiments, and performed data analysis. P. G. R. and G. S. L. developed the thermodynamic model and conducted the theoretical calculations. M. C. supervised the GISAXS and XRR data analysis. O. A. supervised the project.

## Conflicts of interest

The authors declare no competing interests.

## Acknowledgements

This work was supported by CONICET, ANPCyT and Universidad Nacional de La Plata (UNLP). E. P., S. A. and P. G. R. acknowledge CONICET for their scholarships. G. S. L., M. C. and O. A. are staff researchers of CONICET.

## References

- 1 Y. Cui, Q. Wei, H. Park and C. M. Lieber, *Science*, 2001, **293**, 1289–1292.
- 2 H. Li, W. Shi, J. Song, H. J. Jang, J. Dailey, J. Yu and H. E. Katz, *Chem. Rev.*, 2018, **119**, 3–35.
- 3 W. Fu, L. Jiang, E. P. van Geest, L. M. C. Lima and G. F. Schneider, *Adv. Mater.*, 2017, **29**, 1603610.
- 4 A. Zhang and C. M. Lieber, *Chem. Rev.*, 2016, **116**, 215–257.
- 5 Y. Zhao, S. S. You, A. Zhang, J. H. Lee, J. Huang and C. M. Lieber, *Nat. Nanotechnol.*, 2019, **14**, 783–790.
- 6 B. R. Goldsmith, L. Locascio, Y. Gao, M. Lerner, A. Walker, J. Lerner, J. Kyaw, A. Shue, S. Afsahi, D. Pan, J. Nokes and F. Barron, *Sci. Rep.*, 2019, **9**, 1–10.
- 7 D. Rani, V. Pachauri, A. Mueller, X. T. Vu, T. C. Nguyen and S. Ingebrandt, *ACS Omega*, 2016, **1**, 84–92.
- 8 E. Piccinini, C. Bliem, C. Reiner-Rozman, F. Battaglini, O. Azzaroni and W. Knoll, *Biosens. Bioelectron.*, 2017, **92**, 661–667.
- 9 T. Berninger, C. Bliem, E. Piccinini, O. Azzaroni and W. Knoll, *Biosens. Bioelectron.*, 2018, **115**, 104–110.
- 10 M. Á. García-Chamé, Ó. Gutiérrez-Sanz, E. Ercan-Herbst, N. Haustein, M. S. Filipiak, D. E. Ehrnhöfer and A. Tarasov, *Biosens. Bioelectron.*, 2020, **159**, 1–6.

- 11 G. Seo, G. Lee, M. J. Kim, S.-H. Baek, M. Choi, K. B. Ku, C.-S. Lee, S. Jun, D. Park, H. G. Kim, S.-J. Kim, J.-O. Lee, B. T. Kim, E. C. Park and S. Il Kim, *ACS Nano*, 2020, **14**, 5135–5142.
- 12 P. Seshadri, K. Manoli, N. Schneiderhan-Marra, U. Anthes, P. Wierzchowiec, K. Bonrad, C. Di Franco and L. Torsi, *Biosens. Bioelectron.*, 2018, **104**, 113–119.
- 13 J. Choi, T. W. Seong, M. Jeun and K. H. Lee, *Adv. Healthcare Mater.*, 2017, **6**, 1–14.
- 14 E. Piccinini, S. Alberti, G. S. Longo, T. Berninger, J. Breu, J. Dostalek, O. Azzaroni and W. Knoll, *J. Phys. Chem. C*, 2018, **122**, 10181–10188.
- 15 N. Haustein, Ó. Gutiérrez-Sanz and A. Tarasov, *ACS Sens.*, 2019, **4**, 874–882.
- 16 P. Aspermaier, U. Ramach, C. Reiner-Rozman, S. Fossati, B. Lechner, S. E. Moya, O. Azzaroni, J. Dostalek, S. Szunerits, W. Knoll and J. Bintliger, *J. Am. Chem. Soc.*, 2020, **142**, 11709–11716.
- 17 E. Stern, R. Wagner, F. J. Sigworth, R. Breaker, T. M. Fahmy and M. A. Reed, *Nano Lett.*, 2007, **7**, 3405–3409.
- 18 R. Elnathan, M. Kwiat, A. Pevzner, Y. Engel, L. Burstein, A. Khatchourints, A. Lichtenstein, R. Kantaev and F. Patolsky, *Nano Lett.*, 2012, **12**, 5245–5254.
- 19 G. S. Kulkarni and Z. Zhong, *Nano Lett.*, 2012, **12**, 719–723.
- 20 G. S. Kulkarni, W. Zang and Z. Zhong, *Acc. Chem. Res.*, 2016, **49**, 2578–2586.
- 21 N. Gao, T. Gao, X. Yang, X. Dai, W. Zhou, A. Zhang and C. M. Lieber, *Proc. Natl. Acad. Sci. U. S. A.*, 2016, **113**, 14633–14638.
- 22 N. Gao, W. Zhou, X. Jiang, G. Hong, T.-M. Fu and C. M. Lieber, *Nano Lett.*, 2015, **15**, 2143–2148.
- 23 Ó. Gutiérrez-Sanz, N. M. Andoy, M. S. Filipiak, N. Haustein and A. Tarasov, *ACS Sens.*, 2017, **2**, 1278–1286.
- 24 N. M. Andoy, M. S. Filipiak, D. Vetter, Ó. Gutiérrez-Sanz and A. Tarasov, *Adv. Mater. Technol.*, 2018, **3**, 1–12.
- 25 M. Kohmoto, H. Ozawa, L. Yang, T. Hagio, M. Matsunaga and M. A. Haga, *Langmuir*, 2016, **32**, 4141–4152.
- 26 M. Cao, A. Fu, Z. Wang, J. Liu, N. Kong, X. Zong, H. Liu and J. J. Gooding, *J. Phys. Chem. C*, 2014, **118**, 2650–2659.
- 27 J. A. Mann, T. Alava, H. G. Craighead and W. R. Dichtel, *Angew. Chem., Int. Ed.*, 2013, **52**, 3177–3180.
- 28 G. J. A. A. Soler-Illia and O. Azzaroni, *Chem. Soc. Rev.*, 2011, **40**, 1107–1150.
- 29 S. Alberti, G. J. A. A. Soler-Illia and O. Azzaroni, *Chem. Commun.*, 2015, **51**, 6050–6075.
- 30 V. López-Puente, S. Abalde-Cela, P. C. Angelomé, R. A. Alvarez-Puebla and L. M. Liz-Marzán, *J. Phys. Chem. Lett.*, 2013, **4**, 2715–2720.
- 31 M. Chen, W. Luo, Z. Zhang, R. Wang, Y. Zhu, H. Yang and X. Chen, *ACS Appl. Mater. Interfaces*, 2017, **9**, 42156–42166.
- 32 M. B. Serrano, C. Despas, G. Herzog and A. Walcarius, *Electrochem. Commun.*, 2015, **52**, 34–36.
- 33 M. Etienne, A. Quach, D. Grosso, L. Nicole, C. Sanchez and A. Walcarius, *Chem. Mater.*, 2007, **19**, 844–856.
- 34 A. Walcarius, *Chem. Soc. Rev.*, 2013, **42**, 4098–4140.
- 35 A. Calvo, M. C. Fuertes, B. Yameen, F. J. Williams, O. Azzaroni and G. J. A. A. Soler-Illia, *Langmuir*, 2010, **26**, 5559–5567.
- 36 A. Calvo, B. Yameen, F. J. Williams, O. Azzaroni and G. J. A. A. Soler-Illia, *Chem. Commun.*, 2009, 2553–2555.
- 37 A. Brunsen, C. Díaz, L. I. Pietrasanta, B. Yameen, M. Ceolín, G. J. A. A. Soler-Illia and O. Azzaroni, *Langmuir*, 2012, **28**, 3583–3592.
- 38 A. Brunsen, J. Cui, M. Ceolín, A. del Campo, G. J. A. A. Soler-Illia and O. Azzaroni, *Chem. Commun.*, 2012, **48**, 1422–1424.
- 39 A. Brunsen, A. Calvo, F. J. Williams, G. J. A. A. Soler-Illia and O. Azzaroni, *Langmuir*, 2011, **27**, 4328–4333.
- 40 A. Andrieu-Brunsen, S. Micoureau, M. Tagliacuzzi, I. Szleifer, O. Azzaroni and G. J. A. A. Soler-Illia, *Chem. Mater.*, 2015, **27**, 808–821.
- 41 H. Wang, J. Varghese and L. Pilon, *Electrochim. Acta*, 2011, **56**, 6189–6197.
- 42 S. Schmidt, S. Alberti, P. Vana, G. J. A. A. Soler-Illia and O. Azzaroni, *Chem. – Eur. J.*, 2017, **23**, 14500–14506.
- 43 M. G. Bellino, A. E. Regazzoni and G. J. A. A. Soler-Illia, *ACS Appl. Mater. Interfaces*, 2010, **2**, 360–365.
- 44 S. Alberti, *Películas delgadas mesoporosas polímero-inorgánico: uso del confinamiento como herramienta de diseño de nanoarquitecturas híbridas*, PhD Thesis, Universidad de Buenos Aires, Facultad de Ciencias Exactas, 2019.
- 45 S. Dourdain, A. Mehdi, J. F. Bardeau and A. Gibaud, *Thin Solid Films*, 2006, **495**, 205–209.
- 46 E. Piccinini, G. A. González, O. Azzaroni and F. Battaglini, *J. Colloid Interface Sci.*, 2021, **581**, 595–607.
- 47 A. Alvarez-Fernandez, B. Reid, M. J. Fornerod, A. Taylor, G. Divitini and S. Guldin, *ACS Appl. Mater. Interfaces*, 2020, **12**, 5195–5208.
- 48 Z. Di, D. Posselt, D. M. Smilgies, R. Li, M. Rauscher, I. I. Potemkin and C. M. Papadakis, *Macromolecules*, 2012, **45**, 5185–5195.
- 49 E. Piccinini, J. S. Tuninetti, J. Irigoyen Otamendi, S. E. Moya, M. Ceolín, F. Battaglini and O. Azzaroni, *Phys. Chem. Chem. Phys.*, 2018, **20**, 9298–9308.
- 50 D. Babonneau, *J. Appl. Crystallogr.*, 2010, **43**, 929–936.
- 51 E. Piccinini, C. Bliem, J. M. Giussi, W. Knoll and O. Azzaroni, *Langmuir*, 2019, **35**, 8038–8044.
- 52 L. Malfatti, P. Falcaro, A. Pinna, B. Lasio, M. F. Casula, D. Loche, A. Falqui, B. Marmiroli, H. Amenitsch, R. Sanna, A. Mariani and P. Innocenzi, *ACS Appl. Mater. Interfaces*, 2014, **6**, 795–802.
- 53 P. G. Ramírez, M. G. Del Pópolo, J. A. Vila, I. Szleifer and G. S. Longo, *J. Colloid Interface Sci.*, 2019, **552**, 701–711.
- 54 S. H. Behrens and D. G. Grier, *J. Chem. Phys.*, 2001, **115**, 6716–6721.
- 55 H. Bark, M. Ko, M. Lee, W. Lee, B. Hong and H. Lee, *ACS Sustainable Chem. Eng.*, 2018, **6**, 7468–7474.
- 56 N. D. K. Tu, J. Choi, C. R. Park and H. Kim, *Chem. Mater.*, 2015, **27**, 7362–7369.

- 57 Y. Y. Wang and P. J. Burke, *Nano Res.*, 2014, **7**, 1650–1658.
- 58 P. Innocenzi and L. Malfatti, *Chem. Soc. Rev.*, 2013, **42**, 4198–4216.
- 59 Z. Du, W. Chen, Y. Chen, S. Qiao, X. Bao, S. Wen, M. Sun, L. Han and R. Yang, *J. Mater. Chem. A*, 2014, **2**, 15904–15911.
- 60 B. Friedel, P. E. Keivanidis, T. J. K. Brenner, A. Abrusci, C. R. McNeill, R. H. Friend and N. C. Greenham, *Macromolecules*, 2009, **42**, 6741–6747.
- 61 I. Y. Sohn, D. J. Kim, J. H. Jung, O. J. Yoon, T. Nguyen Thanh, T. Tran Quang and N. E. Lee, *Biosens. Bioelectron.*, 2013, **45**, 70–76.
- 62 C. Bliem, E. Piccinini, W. Knoll and O. Azzaroni, in *Enzyme Nanoarchitectures: Enzymes Armored with Graphene*, ed. C. V. Kumar, Elsevier, 2018, pp. 23–46.
- 63 I. Heller, S. Chatoor, J. Männik, M. A. G. Zevenbergen, C. Dekker and S. G. Lemay, *J. Am. Chem. Soc.*, 2010, **132**, 17149–17156.
- 64 W. Fu, C. Nef, O. Knopfmacher, A. Tarasov, M. Weiss, M. Calame and C. Schönenberger, *Nano Lett.*, 2011, **11**, 3597–3600.
- 65 P. Salvo, B. Melai, N. Calisi, C. Paoletti, F. Bellagambi, A. Kirchhain, M. G. Trivella, R. Fuoco and F. Di Francesco, *Sens. Actuators, B*, 2018, **256**, 976–991.
- 66 M. Zhang, C. Liao, Y. Yao, Z. Liu, F. Gong and F. Yan, *Adv. Funct. Mater.*, 2014, **24**, 978–985.
- 67 H. Tang, P. Lin, H. L. W. Chan and F. Yan, *Biosens. Bioelectron.*, 2011, **26**, 4559–4563.
- 68 Y. Huang, X. Dong, Y. Shi, C. M. Li, L.-J. Li and P. Chen, *Nanoscale*, 2010, **2**, 1485–1488.
- 69 S. Alberti, J. Dostalek, G. J. A. A. Soler-Illia, O. Azzaroni and W. Knoll, Polyelectrolyte layer-by-layer assembly into and onto mesoporous thin films: An Optical Waveguide Spectroscopy Study, 2021, submitted.
- 70 R. N. Smith, L. Reven and C. J. Barrett, *Macromolecules*, 2003, **36**, 1876–1881.
- 71 J. Tu, A. L. Boyle, H. Friedrich, P. H. H. Bomans, J. Bussmann, N. A. J. M. Sommerdijk, W. Jiskoot and A. Kros, *ACS Appl. Mater. Interfaces*, 2016, **8**, 32211–32219.
- 72 S. Alberti, S. Schmidt, S. Hageneder, M. Ceolin, P. Vana, G. J. A. A. Soler-Illia, O. Azzaroni, J. Dostalek, W. Knoll and P. C. Angelome, Design and preparation of large-pore mesoporous silica thin films: Size-dependent infiltration of biomolecules in nanoscale pores, 2021, submitted.
- 73 A. B. Artyukhin, M. Stadermann, R. W. Friddle, P. Stroeve, O. Bakajin and A. Noy, *Nano Lett.*, 2006, **6**, 2080–2085.
- 74 B. M. Lowe, C. K. Skylaris, N. G. Green, Y. Shibuta and T. Sakata, *Nanoscale*, 2018, **10**, 8650–8666.